Earth and Planetary Science Letters 560 (2021) 116785

Contents lists available at ScienceDirect

Earth and Planetary Science Letters

www.elsevier.com/locate/epsl

Shear-wave velocity structure beneath Alaska from a Bayesian joint inversion of Sp receiver functions and Rayleigh wave phase velocities

Isabella Gama [a,*], Karen M. Fischer [a], Zachary Eilon [b], Hannah E. Krueger [a], Colleen A. Dalton [a], Lucy M. Flesch [c]

[a] Department of Earth, Environmental and Planetary Sciences, Brown University, Providence, RI, 02912, USA
[b] Department of Earth Sciences, University of California, Santa Barbara, CA, 93106, USA
[c] Department of Earth, Atmospheric, and Planetary Sciences, Purdue University, West Lafayette, IN, 47907, USA

ARTICLE INFO

Article history:
Received 7 August 2020
Received in revised form 10 December 2020
Accepted 23 January 2021
Available online 3 February 2021
Editor: J.-P. Avouac

Keywords:
Sp receiver functions
lithosphere-asthenosphere boundary
Alaska Transportable Array
mantle imaging
Bayesian inversion

ABSTRACT

The present-day lithospheric structure of Alaska is the result of a unique tectonic history of subduction and terrane accretion that controls upper plate thickness and rheology. To provide new constraints on the structure of the crust and upper mantle beneath Alaska, we jointly inverted Sp receiver functions and Rayleigh wave phase velocities to calculate shear-wave velocity profiles. Robust Sp receiver functions were obtained using a broad range of frequencies (2–100 s), time-domain deconvolution, and K-means cluster analysis. Tests of the Bayesian joint inversion with synthetic data illustrate that Sp receiver functions enhance the resolution of the velocity gradients at the Moho and the lithosphere-asthenosphere boundary, while Rayleigh surface waves provide information about absolute velocities. Our results show that in central Alaska, above the shallow slab, the continental lithosphere is thinnest (~60 km) and the asthenosphere has its lowest velocities. This zone coincides with the Denali Volcanic Gap. The continental lithosphere thickens to the north beneath the Brooks Range and the northern Arctic Alaska terrane, reaching values of 110 to 130 km, with high lithospheric velocities that are comparable to Archean cratons. This pattern is consistent with a northward decrease in upper plate modification by melt and volatiles derived from the slab, in addition to intrinsic mantle velocity and viscosity differences between inherited lithospheric terranes. Lithospheric and asthenospheric velocities are not significantly different inside and outside of the Denali Volcanic Gap, but at the boundaries of this region lithospheric thickness increases rapidly to the north and gradually to the south. In the south, the subducting Yakutat plate is thicker (~100–120 km) than the subducting Pacific plate (~80–90 km), likely due to its thicker crust.

1. Introduction

Subduction of the Pacific plate and Yakutat microplate beneath the North American and Bering plates deforms southern Alaskan lithosphere, uplifting mountain ranges such as the Alaska Range (e.g. Jadamec et al., 2013; Finzel et al., 2015) (Fig. 1). In contrast, the lithosphere in northernmost Alaska has been hypothesized to be thicker, stronger and less deformable (e.g. O'Driscoll and Miller, 2015; Finzel et al., 2015). However, uncertainty remains about how the transition between these domains is reflected in continental lithospheric structure and about the role of subduction in modifying the upper plate (e.g. Rondenay et al., 2010). In this study, through joint inversion of surface wave and converted body wave (Sp) data, we obtained new constraints on the seismic velocity structure of the crust and mantle of Alaska in order to better understand the relationship of subduction and the upper plate mantle.

1.1. Alaskan subduction and terrane accretion

The North American plate in Alaska is a complex mosaic of accreted terranes (e.g. Colpron et al., 2007; Fuis et al., 2008; Colpron and Nelson, 2011) (Fig. 1b). At the southern margin of Alaska, the Yakutat terrane is a subducting oceanic plateau with anomalous thick crust (e.g., Fuis et al., 2008; Christeson et al., 2013), while the subducting plate to its west is normal Pacific oceanic lithosphere. Following Colpron et al. (2007) and Colpron and Nelson (2011), the terranes in Alaska and neighboring Canada can be categorized into four major groups (Fig. 1b): i) the lithosphere of ancestral North America, including both the craton and continental margin of Laurentia; ii) peri-Laurentian terranes that largely represent Devonian to Jurassic arcs formed at the margin of ancestral North America;

* Corresponding author.
E-mail address: igama@brown.edu (I. Gama).

https://doi.org/10.1016/j.epsl.2021.116785
0012-821X/

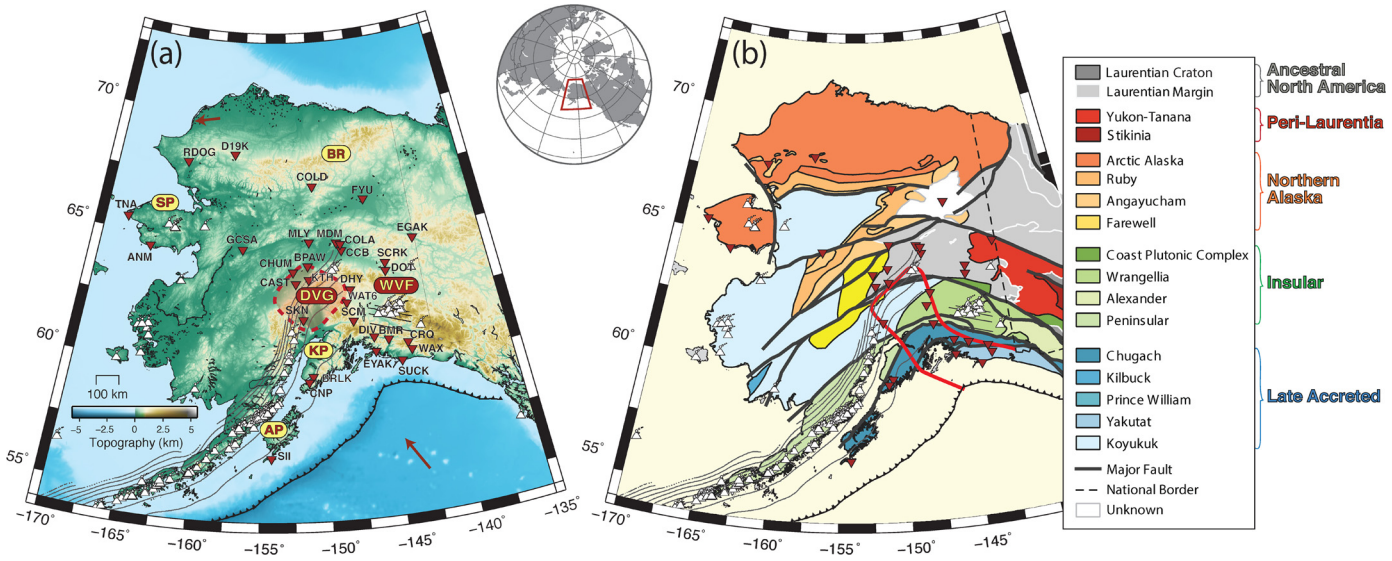

Fig. 1. (a) Regional setting of Alaska plotted on ETOPO1 topography (Amante and Eakins, 2009). Labels with yellow background are: BR = Brooks Range; SP = Seward Peninsula; AP = Alaska Peninsula; and KP = Kenai Peninsula; and labels with red background are: Wrangell Volcanic Field (WVF) and Denali Volcanic Gap (DVG), also marked with the red dashed line. In both figures, red inverted triangles represent the stations employed in this paper with their names (black text) and white triangles are volcanoes (avo.alaska.edu). Grey continuous lines mark seismicity contours from (Hayes et al., 2018) except near the WVF where they are from Kiara Daly, personal communication, 2020. The trench is shown as the black line with ticks. Small red arrows in the northwest and southeast of the map indicate the direction of plate motion in the no-net rotation reference frame (Argus et al., 2011); rates are 45 mm/yr for the Pacific plate, and 23 mm/yr for the North American plate. (b) Tectonic terranes (Colpron et al., 2007; Colpron and Nelson, 2011). Black thick lines are major faults. Red line highlights the bounds of subducted Yakutat crust based on Eberhart-Phillips et al. (2006) as well as the unsubducted Yakutat terrane. (For interpretation of the colors in the figure(s), the reader is referred to the web version of this article.)

iii) the Neoproterozoic to Jurassic Northern Alaska and Insular Terranes, which did not derive from the western margin of Laurentia, but instead from other continents, or possibly from further east in Laurentia in the case of the northern portion of the Arctic Alaska terrane that contains much of the Brooks Range; and iv) the Late Accreted terranes that docked in the late Mesozoic to Cenozoic and include the Yakutat. The various tectonic origins of these terranes likely produced lithosphere with different thicknesses and internal properties, and these properties in turn influence the evolution of the lithospheric blocks.

1.2. Prior seismic studies in Alaska

Numerous previous studies have imaged the crust and mantle structure of Alaska using receiver functions (RFs) (e.g., O'Driscoll and Miller, 2015; Rondenay et al., 2010; Kim et al., 2014; Miller et al., 2018; Zhang et al., 2019), surface wave tomography (e.g., Wang and Tape, 2014; Jiang et al., 2018; Feng and Ritzwoller, 2019), body wave tomography (e.g., Eberhart-Phillips et al., 2006), and SKS splitting (e.g., Venereau et al., 2019; McPherson et al., 2020). Some have combined multiple datatypes that include Ps receiver function data to provide additional constraints on crustal properties within the tomographic inversions (e.g., Ward and Lin, 2018; Martin-Short et al., 2018; Berg et al., 2020). However, to date, none have utilized data capable of capturing mantle velocity discontinuities at high resolution.

In this study we incorporate Sp phases (in the form of Sp receiver functions), ambient noise, and earthquake-based surface waves in a Bayesian approach (Eilon et al., 2018) to solve for crust and mantle structure in Alaska. To our knowledge, this study is the first to combine these types of data in Alaska. With the resulting shear-wave velocity models, we addressed four questions: (1) How do upper plate properties relate to the position of the subducting slab and terrane boundaries? (2) How far north does the influence of subduction extend? (3) How do mantle wedge properties relate to volcanism? (4) What differences are observed between the subducting Pacific plate and thick Yakutat microplate lithospheres?

2. Method

We incorporated seismic data types that offer complementary information in the joint inversion. To constrain absolute velocities, we used fundamental mode Rayleigh wave phase velocities measured from ambient noise and teleseismic earthquakes between periods of 5 and 140 s. To enhance resolution of velocity gradients, in the mantle in particular, but also at the Moho, we used Sp converted phases. Analysis of Sp conversion sensitivity kernels demonstrates these phases are particularly effective at resolving velocity gradients with near-horizontal dips, such as the lithosphere-asthenosphere boundary (LAB) (Hua et al., 2020). Because of the respective strengths of the Sp and surface wave data, the resulting shear-wave velocity profiles contain new information on the depth of the LAB, as well as the average velocity of the lithosphere and the minimum velocities in the asthenosphere.

2.1. Body wave receiver functions

We employed Sp RFs (SV deconvolved from P) in the joint inversions with the primary goal of enhancing the vertical resolution of mantle velocity gradients. Clear Sp RFs are easier to interpret at mantle depths compared to Ps because converted Sp phases arrive before the direct S wave, thus avoiding complications due to crustal reverberations that can occur with Ps RFs (e.g., Eilon et al., 2018). However, we also calculated Ps RFs (P deconvolved from S) to verify that Moho depths from Sp and Ps receiver function stacks are consistent (Fig. S1). One challenge with Sp RFs is that they often have lower signal-to-noise ratios compared to Ps. To improve signal-to-noise ratios in receiver function stacks, we objectively selected RFs using K-means cluster analysis. To avoid artifacts such as side lobes when calculating RFs, we employed both a wide-band filter (2–100 s) that minimizes the introduction of spectral ringing and time-domain deconvolution. The supplemental material contains more detailed discussion of the steps involved in the receiver function calculation.

We analyzed body wave data recorded at 31 permanent stations from the Alaska Regional Seismic Network (AK, doi:https://

doi.org/10.7914/SN/AK), the IRIS Global Seismograph Network (IU, doi:https://doi.org/10.7914/SN/IU), and the USGS Advanced National Seismic System (US, doi:https://doi.org/10.7914/SN/US). We selected stations that had been recording data for over six years to ensure large numbers of body wave arrivals and therefore high-quality receiver function stacks. For additional sampling in northern Alaska, we also analyzed data from station D19K from the NSF EarthScope Transportable Array (TA, doi:https://doi.org/10.7914/SN/TA). The data from D19K indicate the promise of TA data for this type of joint inversion. However, because initial Sp receiver functions at a number of other TA stations had lower signal-to-noise ratios, joint inversions involving data from all Alaska TA stations are planned for the future when more events will have been recorded.

The waveforms in this study represent events with $Mw > 5.7$, depths <100 km, and epicentral distances of 55°–80° for Sp (and 35°–80° for the Ps examples shown in the supplement). We grouped Sp and Ps phases into geographic clusters over 30° of back-azimuth. The resulting stacks of receiver functions for these back-azimuthal slices represent average velocity structure over more limited geographical regions than would a stack for all back-azimuths, resulting in better lateral resolution of shear-wave velocity structure when the receiver function stacks are incorporated in the joint inversion. The distribution of back-azimuths is dominated by two groups, 220–250° (southeast Pacific events) and 250–280° (north and northwest Pacific events).

Examples of Sp RFs (Fig. 2 and Fig. S1) reveal a clear phase from a velocity increase in the time range expected for the Moho conversion (3–6 s), and another phase from a negative velocity gradient in the time range predicted for a conversion at the transition between lithosphere and asthenosphere (6–12 s). The example RF stacks in Fig. 2 are migrated to depth with the SEMum2 model (French et al., 2013) to illustrate observed phase depths, and RFs are shown both in time and depth in Fig. S1. When used in the inversion, the RFs are treated as functions of time. The times/depths of the potential LAB velocity gradients vary geographically, with phase peaks (which approximate gradient mid-point depths) ranging from 60 km to 120 km assuming the SEMum2 model for migration (French et al., 2013).

2.2. Surface wave phase velocities

We used fundamental mode Rayleigh wave phase velocities for Alaska obtained from ambient noise and earthquake sources. For Rayleigh waves generated by earthquakes, we followed the approach used by Babikoff and Dalton (2019). Travel times in the period range of 25–140 s were measured with interstation cross-correlation using the Automated Shear Wave Measurement System (Jin and Gaherty, 2015), and phase-velocity maps were determined with the Eikonal wavefront-tracking approach (Lin et al., 2009). For the joint inversions we also incorporated ambient noise phase velocities for periods from 5 to 25 s, following the approach of Ekström et al. (2009).

Rayleigh wave phase velocity maps (Fig. 3) reveal distinct regional variations. At periods of 25 s, where sensitivity is primarily within the crust, the lowest velocities occur beneath volcanically active regions in southern Alaska and the Brooks Range in northern Alaska. At longer periods, higher velocities occur in the vicinity of the northwest-dipping subducting lithosphere as well as in northern Alaska.

2.3. Bayesian joint inversion

We employed a transdimensional hierarchical Bayesian approach to determine robust and smooth 1D shear-wave velocity models beneath each station using a modified version of the framework developed by Eilon et al. (2018). In each iteration, we created a synthetic Earth velocity profile, predicted the corresponding Sp converted phases and Rayleigh wave dispersion curves, and calculated the misfits of these predictions relative to the observed Sp RFs and Rayleigh wave phase velocities. A Monte Carlo Markov Chain (MCMC) search probed the model parameter space by randomly perturbing model parameters, and using a Metropolis Hastings criterion (e.g. Hastings, 1970), models were accepted if their misfits were lower than in the previous iteration, but models with higher misfits were also accepted with a probability that declined with increasing misfit. This approach created an ensemble of models within acceptable misfit levels. These steps are explained in the following sections.

2.3.1. Model parameterization

We parameterized our models with adaptive discontinuous cubic B-spline functions, one set for the crust and one set for the mantle, to capture both smooth and sharp velocity variations. We solved for the isotropic velocity coefficients for each spline, the number and depth of spline knots, the depth and velocity contrast at the Moho, and hyperparameters that describe the relative uncertainties of the different data types. In the mantle, both negative and positive shear-wave velocity gradients were allowed, but in the crust only models with positive shear-wave velocity gradients were accepted. This latter constraint does not significantly alter the shear-wave velocity profiles in most cases, in part because the Sp receiver functions typically do not contain crustal phases that correspond to negative velocity gradients. Nodes were allowed to increase in number for depths up to 200 km to enable the resolution of sharper velocity gradients, but adjacent spline knots could not be closer than 3 km. A single value of Vp/Vs in the crust was a free parameter, but we fixed this value in the mantle at each depth following the AK135 reference model (Kennett et al., 1995). The ratio of density to Vs in the crust was defined after Brocher (2005) and in the mantle after Abers and Hacker (2016).

2.3.2. Forward modeling

To calculate synthetic Sp phases for each model, we generated synthetic waveforms using the propagator matrix algorithm (Keith and Crampin, 1977). A dominant source period of 2 s and a ray parameter equal to the mean ray parameter of the stacked Sp phases were assumed. The synthetic data were processed in a manner that was identical to that applied to individual traces in the real data, resulting in filtered P and SV components. In practice, the final step of deconvolving the SV component from the P component was omitted for the synthetics to improved computational efficiency. This choice does not bias the inversions (Figs. S2 and S3). The timing and relative amplitudes of the phases in the non-deconvolved synthetics are identical to those after deconvolution. Thus, omitting deconvolution from the synthetics only eliminates what amounts to a filtering operation. The effects of including deconvolution in the observed data processing are discussed further in Section 2.4.

The synthetic P and SV components typically have greater short period content than the observed Sp RFs, but this is accounted for by the form of the body wave misfit function employed in the inversion. This misfit function, $\Phi_{\mathrm{Sp}}(m)$, is defined as:

$$\Phi_{\mathrm{Sp}}(m) = \left\| \left[\mathrm{P}_p(t,m) * \mathrm{SV}_{\mathrm{auto}}(t) \right] - \left[\mathrm{SV}_p(t,m) * \mathrm{SpRF}(t) \right] \right\|^2$$

where P_p and SV_p are the predicted P and SV components, SpRF is the stack of observed Sp receiver functions, and $\mathrm{SV}_{\mathrm{auto}}$ is the stack of the auto-deconvolved observed SV time series. Both terms in the misfit function contain cross-convolutions of observed and synthetic data, thus removing the need for observed and synthetic data to have the same period content. When calculating misfit,

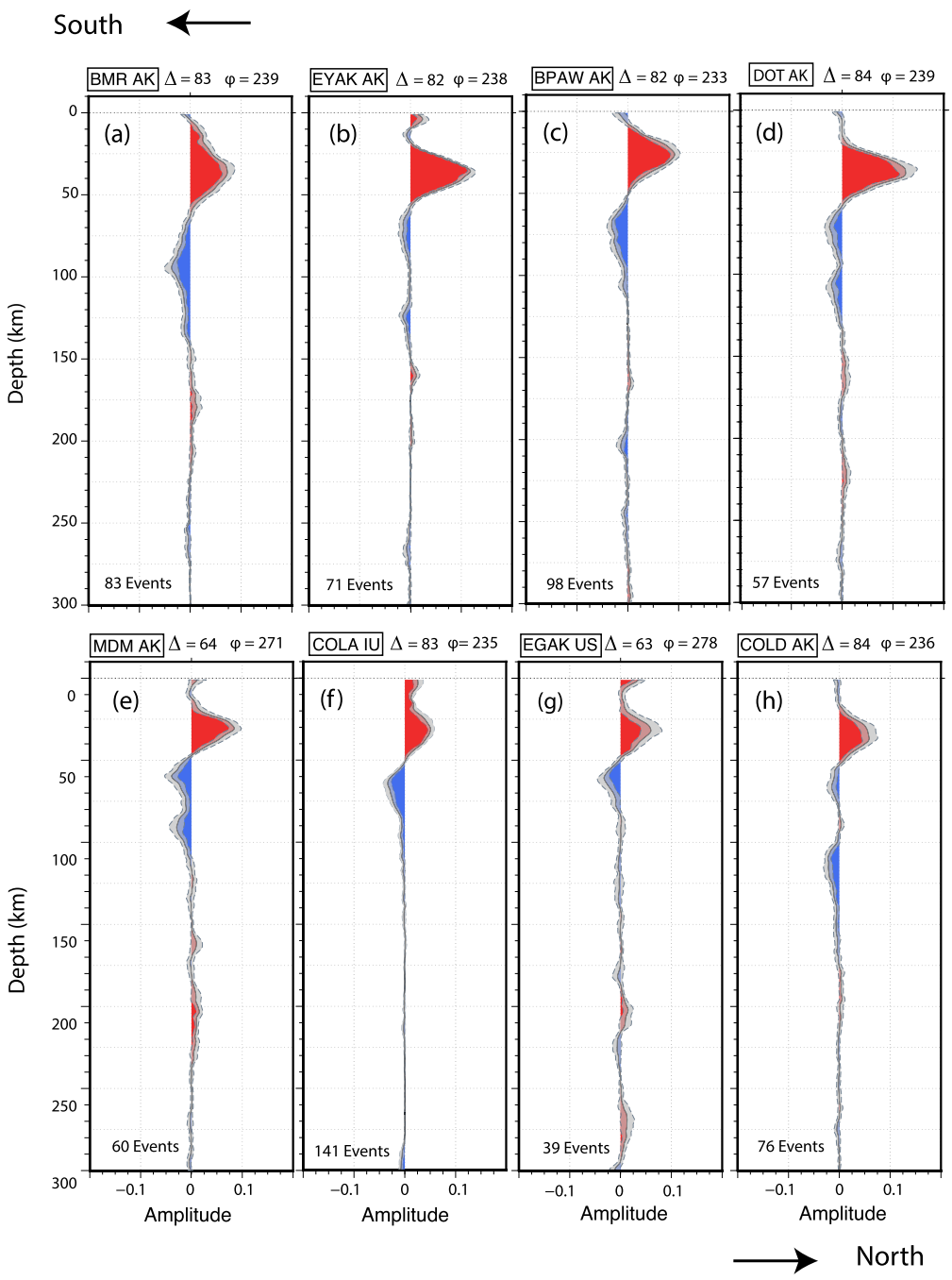

Fig. 2. Examples of Sp receiver function stacks. Colored regions show the median of weighted individual receiver functions; grey shading shows one standard deviation uncertainties. Sp receiver functions were flipped to have the same polarity as Ps. Mean distance (Δ) of the events, number of events, and mean back-azimuth (φ) appear above each panel. Stations are shown from southern (upper left) to northern Alaska (lower right). Positive (red) phases in the 30–40 km depth range correspond to the Moho; negative (blue) phases in the shallow upper mantle are potential LAB phases. Receiver functions in this figure were migrated to depth with the SEMum2 velocity model (French et al., 2013).

we used a −36 to −1 s range (note reversed time window with 0 s being the S arrival) that contained the Moho and LAB phases for Sp. We normalized the amplitudes of the Moho phases in the observed Sp receiver function and the predicted SV waveforms to 1. The contribution of each point in time to the misfit was weighted by empirically determined bootstrap errors for the observed RFs.

We calculated synthetic fundamental-mode Rayleigh wave phase velocities using the Mineos algorithm from Computational Infrastructure for Geodynamics (Masters et al., 2011). Because Mineos requires 1-D Earth models over the full radius of the Earth, the velocity models used for the forward calculation of Rayleigh wave phase velocities included the model being tested in the 0–300 km depth range, and the PREM model (Dziewonski and Anderson, 1981) from 400 km to the center of the Earth, with a gradient between the two models in the 300–400 km depth range. To optimize running time, we avoided directly calculating phase velocities from Mineos at each iteration. Instead, at each period in the data, we calculated perturbation kernels for Vp, Vs and density, all varying with depth. Perturbations in phase velocity were then determined by integrating the kernels with velocity and density perturbations over depth. Kernels were updated when changes in model parameters were sufficiently large. Eilon et al. (2018) describe thresholds and tests of this process in detail.

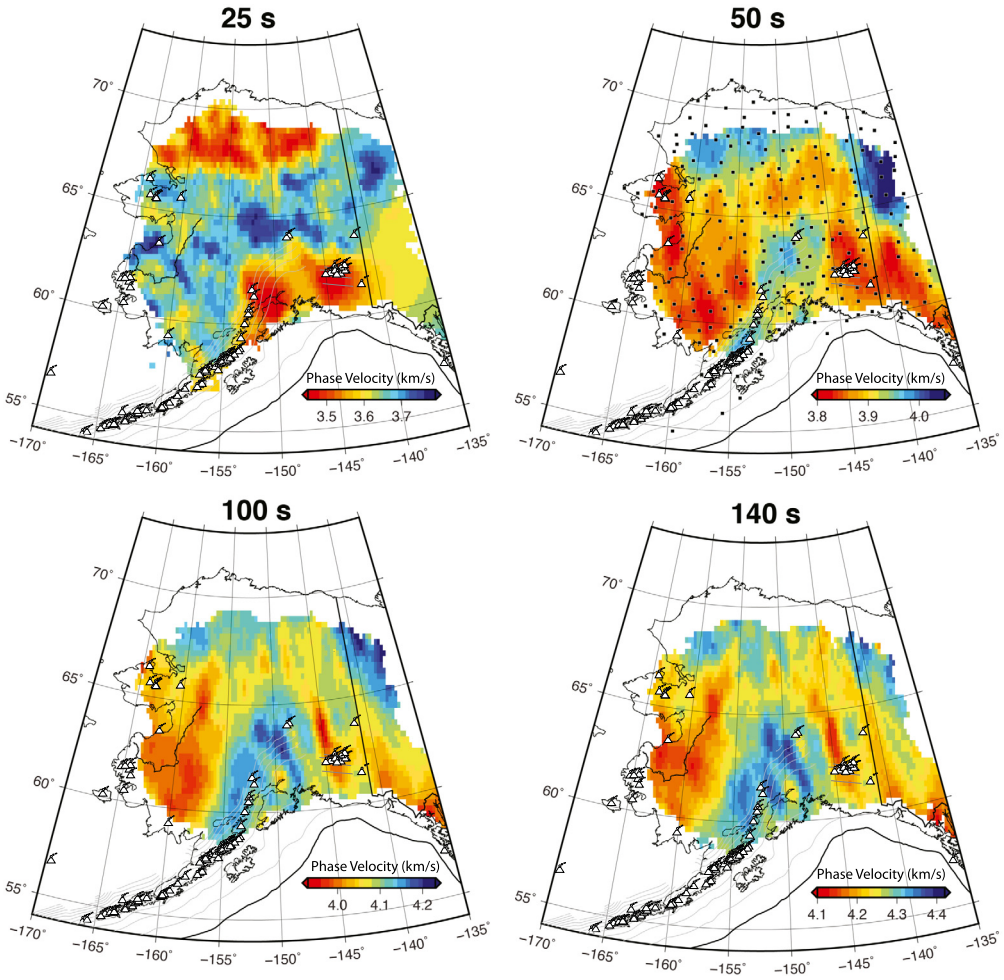

Fig. 3. Rayleigh wave phase velocity maps with absolute velocities (km/s) for periods of 25 s, 50 s, 100 s, and 140 s. Pixels are shown only if more than 120 measurements contributed to the median phase velocity at that location for periods of 50 s, 100 s, and 140 s. Stations used in calculating phase velocities are shown by small black squares in the 50-s map. Seismicity contours and volcanoes are plotted as in Fig. 1.

The surface wave misfit function is defined as:

$$\Phi_{sw} = \left\| C(f) - c_p(f, m) \right\|^2$$

where C and c_p are observed and predicted phase velocities for each frequency, respectively.

2.3.3. Inversion

We evaluated each candidate model using the posterior probability $p(m|d_{obs})$:

$$p(m \mid d_{obs}) \propto p(m) \times p(d_{obs} \mid m)$$

where $p(m)$ is the prior probability for a given model parameter and $p(d_i|m)$ is the likelihood function. The prior distributions for all parameters were determined empirically (Eilon et al., 2018), approximately uniform, and circumscribed by bounds given in Table S1. The likelihood function is defined as:

$$p(d_i \mid m) = \frac{1}{\sqrt{(2\pi\sigma_i)^n}} \times \exp\left(\frac{-\phi_i}{2\sigma_i^2}\right)$$

where ϕ_i is the misfit for each data type described in Section 2.2, and σ_i is the data error hyperparameter that controls the relative weights of the misfits for each data type. The degrees of freedom, n, for surface waves are the number of frequencies in the dispersion curves. For body waves, we estimated the degrees of freedom by using the first zero-crossing of the data auto-correlation function. We measured the total likelihood function for a given model as the product of likelihoods for both of the two data types.

$$p(d_{obs} \mid m) = p(d_{Sp} \mid m)\, p(d_{SW} \mid m)$$

We searched the parameter space using a Monte Carlo Markov Chain (MCMC) approach (e.g., Mosegaard and Tarantola, 1995) run on six independent parallel chains. Each chain was initiated with a model whose parameters were randomly selected from the prior distributions ($p(m)$) (Table S1). The models tested in subsequent iterations were obtained by perturbing a single model parameter by a random value drawn from a Gaussian distribution. Probabilities for perturbing a given parameter type appear in Table S1. Each chain contained twenty thousand iterations. The first eight thousand iterations represented a burn-in period with a rapid increase in likelihood and decrease in misfit. These iterations included a decaying "thermal parameter" that multiplied the standard deviation of the Gaussian distribution from which parameter perturbations were drawn, increasing parameter variations early in the chain and avoiding confinement of the search within local minima (Eilon et al., 2018). The thermal parameter also multiplied the likelihood that a model would be accepted, enhancing model acceptance early in the chain. In each iteration, we accepted or rejected models using a Metropolis-Hastings acceptance criterion (Hastings, 1970). In the burn-in period, models were not saved to the final ensemble. After the burn-in period, likelihood values

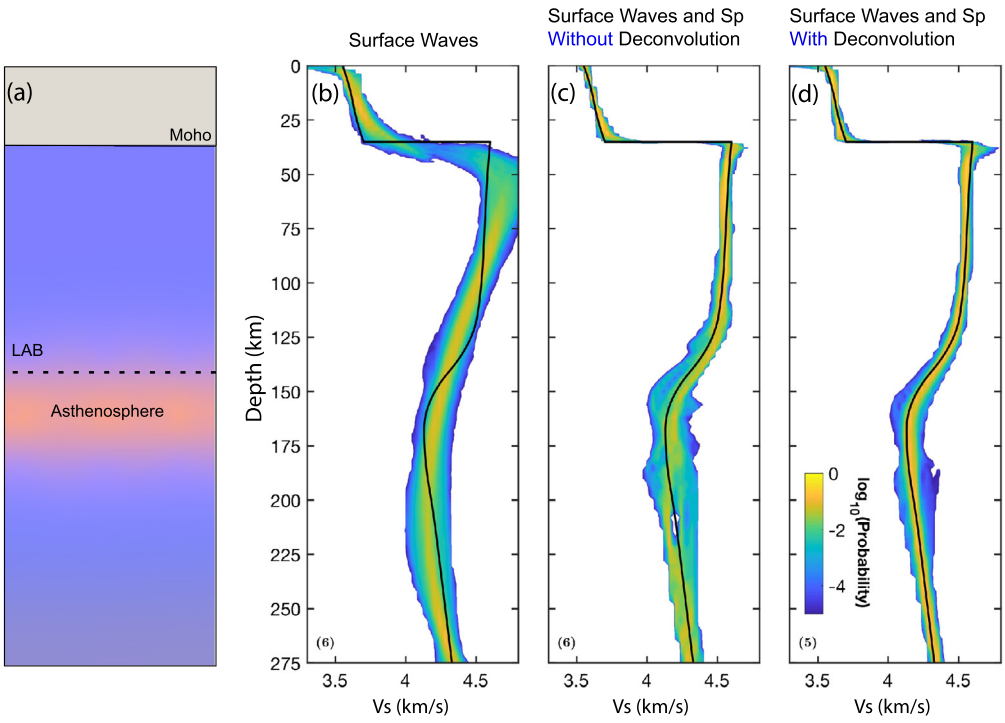

Fig. 4. (a) Schematic of velocity structure used in synthetic test of inversion with a sharp change in velocity at the Moho and a gradual decrease in velocity in the LAB. (b–d) The posterior probability of tests performed (colors) and the Vs model used to generate synthetic data (black). (b) Inversion of surface waves only; (c) surface waves and Sp without deconvolution; and (d) surface waves and Sp with deconvolution.

were high and steady, and we saved the accepted models every 30 iterations. We summed the posterior distribution from all accepted chains to form a final probability distribution. The final velocity model was defined as the median shear-wave velocity at each depth, and crustal Vp/Vs and Moho depth were defined by their median values. Median values were chosen to reduce the influence of outlier accepted models. Uncertainties were represented by 95th and 68th percentile values.

2.4. Tests with synthetic data

In earlier applications of a similar inversion procedure (Eilon et al., 2018), stacks of P and SV waveforms (without deconvolution) were employed, in contrast to the Sp RFs used here. To evaluate the impact of adding deconvolution with the observed waveforms, we conducted inversions with synthetic data both with and without deconvolution. For an input velocity model that resembles some of the inversion results we obtained for stations in northern Alaska (e.g. the black line in Fig. 4) synthetic waveforms were calculated with the same propagator matrix method used in the forward calculation steps of the inversion (Keith and Crampin, 1977). Synthetic waveforms were converted to P and SV components, and then to Sp RFs and auto-deconvolved SV components, using the same procedures that were applied to the real data (Section 2.1). Before deconvolving we added white Gaussian noise with constant standard deviation of $\sigma = 0.02$ to the synthetics. Fundamental mode Rayleigh wave phase velocities were calculated for the input velocity model using Mineos (Masters et al., 2011) with Gaussian noise standard deviation of $\sigma = 0.01$. The synthetic data were inverted using the process described in Section 2.3.

The inversion with only synthetic surface wave phase velocities produces a Vs model probability distribution (colors in Fig. 4b) where the most likely models have absolute velocities that are similar to the input model, but the velocity increase at the Moho is not captured accurately, resulting in over-estimation of Vs in the shallow mantle lithosphere. In addition, the LAB velocity gradient that lies at depths of 130 km to 160 km in the input model is not captured, and instead Vs gradually decreases from approximately 75 km to 175 km.

In contrast, when Sp phase information is added to the inversions (Fig. 4c and 4d), the depths and velocity gradients at the Moho and LAB are well-resolved, highlighting the importance of the Sp data for constraining these boundaries. In the case where Sp RFs represent observed P phases, and the auto-deconvolved SV components represent observed SV phases, the resulting distribution of velocities at mantle depths close to the LAB gradient match the input model better (Fig. 4d) than in the case without deconvolution (Fig. 4c). This difference is likely due to the additional filtering introduced by the deconvolution operation. While the Gaussian noise in the non-deconvolved P and SV components creates greater possibilities for spurious phases to be fit by models that diverge from the input structure, this noise was largely removed in the deconvolution operation. Despite the differences in the frequency content of the deconvolved "data" and the non-deconvolved predicted waveforms used in the inversion in Fig. 4d, the cross-convolution misfit calculation enables good resolution of the input model. Diagnostics from the inversions with the deconvolved synthetic data and the other cases indicate the stability and accuracy of the inversion process (Figs. S2–S4). Inversions with Sp data without surface waves, which are shown in Eilon et al. (2018) but not in this paper, resolve velocity gradients at depths similar to those in the input model, but fail to accurately constrain absolute Vs.

3. Results

3.1. Measuring properties of the lithosphere and asthenosphere

In the shear-wave velocity models obtained by taking the mean of the models accepted in the Bayesian joint inversion, the Moho discontinuity is marked by a sharp increase in velocity. At mantle depths, we typically observe a layer with higher velocities, which

we interpret as the mantle lithosphere, over a lower velocity layer which is consistent with the asthenosphere. In many cases, a second local maximum in velocity occurs at depths of 150 km to 250 km (Fig. 6).

We measured several properties that characterize the lithosphere and asthenosphere from the Vs profiles (Fig. 6): (i) the thickness of the lithosphere, (ii) the depth of the crust-mantle boundary or Moho, (iii) the average velocity in the lithosphere and (iv) the minimum velocity in the asthenosphere. To capture variations in the depth of the negative velocity gradient from lithosphere to asthenosphere, we defined the thickness of the lithosphere (i.e. LAB depth) as the mid-point between the maximum velocity in the mantle lithosphere (measured at depths starting 10 km below the Moho) to the next velocity minimum, as marked in Fig. 6 by the grey dashed line and red squares, respectively. LAB depth uncertainties correspond to 25% of this measurement depth range. LAB depths measured from the joint inversion shear-wave velocity in many cases differ from the depths of LAB phase peaks on the Sp RFs shown in Fig. 2 and Fig. S1, although their uncertainty ranges overlap. These discrepancies are expected, because the Sp RFs in these figures were migrated with the SEMum2 model (French et al., 2013) which differs from the results of the joint inversion, and because predicted Sp phase depths are influenced by the shape of a velocity gradient and will not necessarily lie exactly at its mid-point depth.

We defined the minimum velocity in the asthenosphere as the average within 5 km of the velocity minimum. Moho depths were determined as a parameter in the inversion as explained in Section 2.3.1, with 2σ error bounds, and are characterized by a large positive velocity jump in the Vs profiles, as seen in Figs. 4 and 6. We calculated the average velocity in the lithosphere by taking the mean of the velocities in the profile between the Moho and the determined LAB depths. Moho, lithosphere, and asthenosphere parameter values for each station appear in Table S2.

3.2. Regional patterns in shear-wave velocity

Our shear-wave velocity profiles and the parameters measured from them show distinct regional patterns. In this section, we describe observed patterns in all parameters and compare Moho and LAB depths to previous converted wave and active source studies. Further discussion of the parameter patterns and their origins appears in Section 4.

Moho depths vary significantly across the region (Fig. 7a). In central Alaska, at the northern edge of the subducting slab, the crust is relatively thin (<30 km) with the exception of one station, and its thickness increases modestly to the north and east, for example reaching values of 30 to 35 km beneath the Brooks Range. This northward thickening is consistent with active source studies (e.g. Fuis et al., 2008). Apparent Moho depths are 35 to 40 km where the Yakutat block is thought to have subducted (red outline, Fig. 7a; Fuis et al., 2008), with the exception of the two southeastern stations (AK.WAX, AK.SUCK) which have very shallow Moho depths. Beneath the southern Kenai peninsula, stations AK.BRLK and AK.CNP indicate relatively thick crust (35 km to 42 km), although they lie outside the limits of thick Yakutat crust as constrained by offshore active source data (Fuis et al., 2008). Finally, the crust is thin (~25 km) beneath the Alaska Peninsula in the southwest where the Pacific plate is subducting.

The overall pattern of crustal thickness obtained in the inversions is similar to the large-scale variations in crustal thickness obtained with Ps phases in Zhang et al. (2019) and Miller et al. (2018). For 18 of the 26 stations with crustal thickness values in this study and in Zhang et al. (2019), or 20 of the 28 stations in this study and Miller et al. (2018), our Moho depths are within 5 km of the values in the other studies, taking into account our uncertainties. At the other stations, the crustal thicknesses in this study are smaller, with one exception. The average absolute difference between our Moho depths (including their uncertainties) and those from Zhang et al. (2019) is 3.5 km ± 3.3 km (one standard deviation), and between our results and Miller et al. (2018) the average absolute difference is 4.2 km ± 5.1 km. These Sp versus Ps discrepancies are similar to the average intra-Ps difference between Zhang et al. (2019) and Miller et al. (2018) Moho depths.

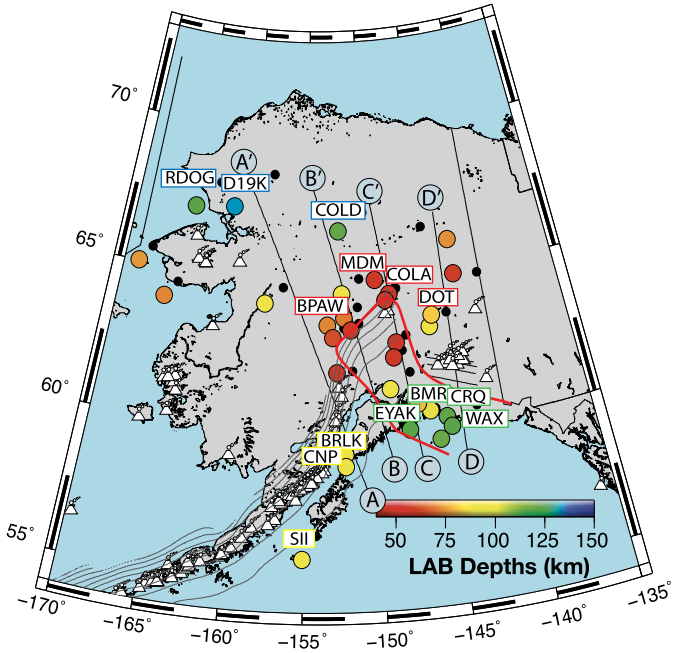

Fig. 5. Map of LAB depths shown by colored points plotted at phase conversion points. Black dots are station locations. Seismicity contours and volcanoes are plotted as in Fig. 1. Yakutat block is outlined in red. Thick black lines show cross-sections in Fig. 8 and labels highlight the stations with Vs profiles plotted in Fig. 6.

LAB depths vary coherently over broad regions (Fig. 5). For instance, the northernmost group of stations (TA.D19K, AK.COLD, and AK.RDOG), which lie in the margins of the Brooks Range (Fig. 1a), in and near the northern Arctic Alaska terrane (Fig. 1b), manifest the thickest lithosphere (118 km to 132 km), while stations in central Alaska have the thinnest lithosphere (45 km to 91 km), including stations on the west coast of the Seward Peninsula whose conversion points sample the offshore continental plate (AK.TNA and AK.ANM). In southern Alaska, where LAB velocity gradients mark the base of the subducting lithosphere, the LAB depths for the Yakutat plate (whose outline is shown in Fig. 1b) range from 79 km to 122 km. The values at the upper end of this range, which correspond to the Sp conversion points that sample farthest offshore, are significantly larger than those observed at the base of the subducting Pacific plate to the west (91 km to 98 km). Both the thickening of lithosphere from central Alaska to northern Alaska, and the thicker lithosphere associated with the subducting Yakutat terrane relative to the Pacific plate, were observed in the Sp receiver function stacking of O'Driscoll and Miller (2015).

Minimum asthenospheric velocities follow broad regional patterns (Fig. 7c). The lowest asthenospheric velocities (<4.3 km/s) are found across central Alaska where the lithosphere is thinnest, including the Seward Peninsula. The average of the minimum asthenospheric velocities for this region (4.30 km/s ± 0.07 km/s) is lower than the average for the remaining regions of Alaska (4.42 km/s ± 0.07 km/s). The highest asthenospheric velocities occur beneath the Brooks Range in the northern portion of the Arctic Alaska terrane (TA.D19K) and beneath the lithosphere subducting under the Kenai Peninsula (AK.BRLK and AK.CNP) (Fig. 6d and Fig. 7c).

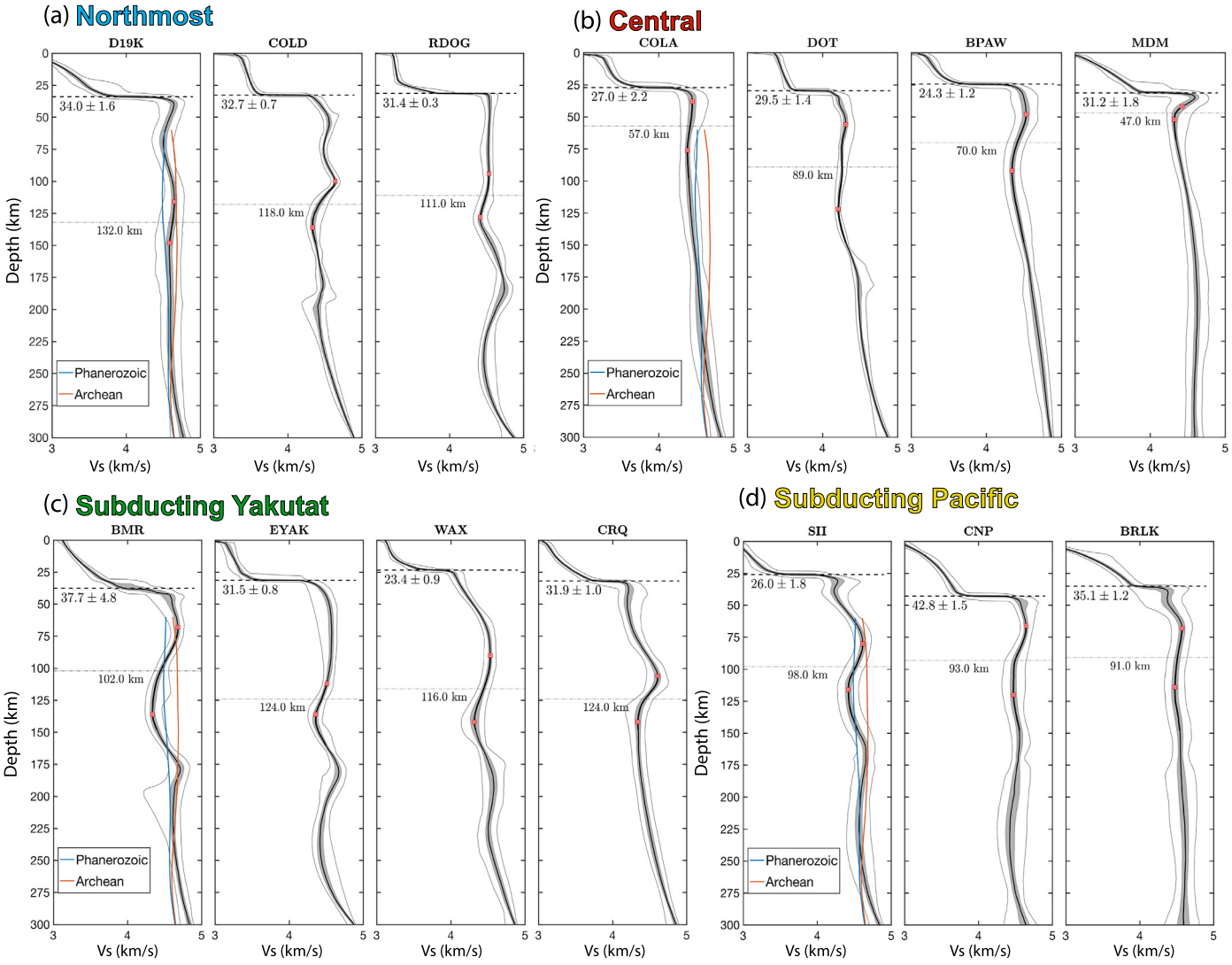

Fig. 6. Isotropic shear-wave velocity profiles. Black lines are the average models and grey lines are 2σ bounds. (a–d) Groups of profiles sample different Alaskan geographic regions. Overlaid lines are Vs from global model SEMum2 averaged by the age of the continental crust, Phanerozoic (blue) and Archean (red) on the first profiles of each region. Red squares mark the maximum velocity in the mantle lithosphere (starting 10 km below the Moho) and the minimum velocity in the asthenosphere; grey dashed line is LAB depth defined as the mid-point of this depth range. Black dashed line is Moho depth.

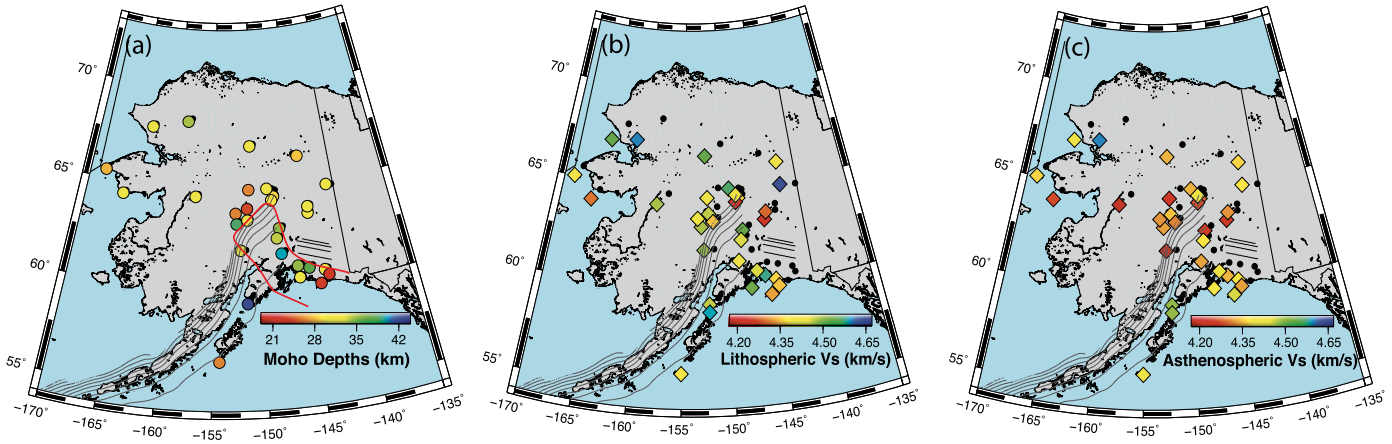

Fig. 7. (a) Map of Moho conversion points from the shear-wave velocity profiles. Yakutat block is outlined in red. Maps of velocities in the (b) lithosphere and (c) asthenosphere. Black dots are the station locations. The velocities are plotted at the lithosphere-asthenosphere boundary conversion points to facilitate the comparison with the calculated LAB depths. Therefore, the average lithospheric velocities correspond to a depth range for which conversion points would plot closer to the station and the minimum asthenospheric velocities are from a depth range for which conversion points are farther from the station. Seismicity contours are plotted as in Fig. 1.

Values for average velocity in the mantle lithosphere in some cases vary significantly at short spatial scales, but two aspects of their distribution stand out. We observe the lowest mantle lithosphere velocities at the eastern edge of the subducting lithosphere (∼4.25 km/s). In addition, the three northern stations with the thickest lithosphere have relatively high average lithospheric velocities (>4.55 km/s).

A final observation from the Vs profiles is that some of them contain local maxima at ∼175 km. These features are particularly pronounced under the slab offshore (Fig. 6c–d) but are also seen further north (Fig. 6a).

4. Discussion

The first-order features of the shear-wave velocity models obtained by the Bayesian joint inversions are that the lithosphere in northern Alaska near the Brooks Range is significantly thicker than in central Alaska, and that asthenospheric velocities are low in a broad band beneath the thin lithosphere of central Alaska, including the Seward Peninsula. Similar patterns are echoed in numerous studies (e.g., Wang and Tape, 2014; O'Driscoll and Miller, 2015; Martin-Short et al., 2018; Jiang et al., 2018; Ward and Lin, 2018; Feng and Ritzwoller, 2019; Berg et al., 2020). In addition, the shear-wave velocity models indicate a greater maximum thickness for the subducting Yakutat plate than for the subducting Pacific plate, as also observed in O'Driscoll and Miller (2015) and Martin-Short et al. (2018). However, while some of the major features of the shear-wave velocity models obtained in this study are consistent with prior work, our use of Sp phases provides narrower constraints on LAB depths than would be possible with surface waves alone, and the estimates of absolute shear-wave velocities in the lithosphere and asthenosphere that honor the LAB depths would not be possible with converted waves alone. In this section, we discuss the implications of these results for upper plate modification by subduction-related processes in the mantle wedge, and the characteristics of the subducting Pacific and Yakutat plates.

4.1. Interactions between subduction-related processes and the upper plate

The broad band of thin lithosphere and low velocity asthenosphere that stretches across central Alaska is easily interpreted as a signature of subduction. Low asthenospheric velocities likely reflect high temperature mantle entrained into the mantle wedge by the subducting slab, slab fluid flux into the mantle wedge (although the competing roles of water and grain size on mantle wedge velocities are debated, e.g. Abers et al., 2014), and possibly the presence of partial melt (e.g. Rondenay et al., 2010; Rodríguez-González et al., 2012). Rising slab fluids and/or partial melt, potentially in combination with shallowing asthenospheric flow lines, in turn provide a mechanism to thin the upper plate lithosphere. This interpretation is supported by the correlation of thin upper plate lithosphere and surface magmatism, as seen in cross-sections A and C in Fig. 8 and beneath the Seward Peninsula (Figs. 1a and 5). The zone of thin lithosphere and low asthenospheric velocities lies landward of the low-attenuation, and presumably cold, wedge corner imaged by Stachnik et al. (2004). The thin lithosphere correlates with a region of particularly high horizontal surface strain rate (Finzel et al., 2011), and is consistent with the idea that the thinner lithosphere is weaker and more easily deformable. Comparison of apparent LAB depths with slab seismicity indicates that the mantle velocity reductions at two stations (AK.DHY and AK.WAT6, Fig. 8c) likely represent a slab-related interface that corresponds to a decrease in velocity with depth.

The lithosphere of northernmost Alaska poses a stark contrast. Beneath the Brooks Range and the northern Arctic-Alaska terrane (Fig. 1) the lithosphere not only reaches thicknesses of ∼130 km (Fig. 8a–b), it also contains shear-wave velocities (stations TA.D19K and AK.COLD, Fig. 6a) that are comparable to the global average for Archean cratons from the SEMum2 model (French et al., 2013). These seismic properties match other geophysical data in the northern Arctic-Alaska terrane that are typical of cratonic lithosphere, including low heat flow (except near the northern coast (Saltus and Hudson, 2007; Batir et al., 2016)) and a zone of high magnetization in the deep crust that has been interpreted as evidence for cold lithosphere (Saltus and Hudson, 2007). These properties have led to the conclusion that the thick northern Alaska lithosphere represents high viscosity mantle (e.g. Finzel et al., 2015). The apparent contrasts in lithospheric thickness and viscosity between northern and central Alaska are in turn important for focusing tractions from asthenospheric flow and predicting surface deformation that matches southward directed surface deformation (Finzel et al., 2015).

Within the subduction modified upper plate lithosphere of central Alaska, the origin of the Denali Volcanic Gap (DVG) has been a topic of debate. The DVG is an area that lies above subducting slab seismicity, yet has lacked significant volcanism since the Miocene (Fig. 1a) and is spatially correlated with the outline of the subducting Yakutat terrane (Fig. 1b). To explore implications for the DVG, we compared shear-wave velocity model properties for a group of stations whose Sp stack mean conversion points lie within the DVG (AK.CAST, AK.BPAW, AK.CHUM, AK.KTH, AK.MLY) to stations whose conversion points lie outside the DVG but at a similar location with respect to slab seismicity contours (AK.MDM, IU.COLA, AK.CCB, AK.SKN). Minimum asthenospheric velocities and average lithospheric velocities do not differ significantly between the two groups. Comparing average values within the DVG to those outside the DVG, asthenospheric velocities are 4.30 ± 0.06 km/s versus 4.30 ± 0.09 km/s, respectively, and lithospheric velocities are 4.43 ± 0.05 km/s versus 4.45 ± 0.09 km/s, respectively.

In contrast, variations in LAB depth do show DVG-related contrasts. Inside the DVG, the LAB lies at depths of 50–60 km directly above slab seismicity located at 140 km depth, in agreement with a sharp reduction in shear-wave velocity imaged and interpreted as pooled partial melt by Rondenay et al. (2010) (Fig. 8b). However, 70 km north from the deepest seismicity along the cross-section, the LAB deepens to approximately 70 km in depth (although this is not technically resolved given the generous error bars on LAB depth) and by 150 km from the deepest seismicity, the LAB has reached a depth of 90 km (AK.MLY). In contrast, on the cross-section on the eastern side of the DVG (Fig. 8c) the LAB appears to remain at a depth of approximately 50 km to a distance of 70 km from the deepest seismicity (AK.MDM). This difference in LAB topography can also be seen on the LAB depth map in Fig. 5.

In some models for the DVG, low angle subduction of the Yakutat terrane beneath the DVG cools the top of the mantle wedge (Rondenay et al., 2010; Martin-Short et al., 2018). For example, Rondenay et al. (2010) propose that this cooling reduces upward flow of warm asthenosphere where the arc would otherwise be located, and instead causes melt to pond below the upper plate at a depth of approximately 60 km somewhat farther landward. Our results are consistent with this model, in the sense that we do observe a shallow LAB where Rondenay et al. (2010) predict ponded melt. One caveat is that volcanoes are present to the northeast of the DVG (Fig. 8c) where the angle of subduction is comparably low to that in the DVG. However, these volcanoes may be explained by their proximity to the edge of the slab, assuming the interpretation of seismicity we employ in this study (e.g. Kiara Daly, personal communication, 2020). Alternatively, upper plate thickness, for example the significantly thicker lithosphere in northern Alaska, may contribute to the shallow Yakutat slab dip, as opposed to attributing the shallow dip to the buoyancy of thick Yakutat crust alone.

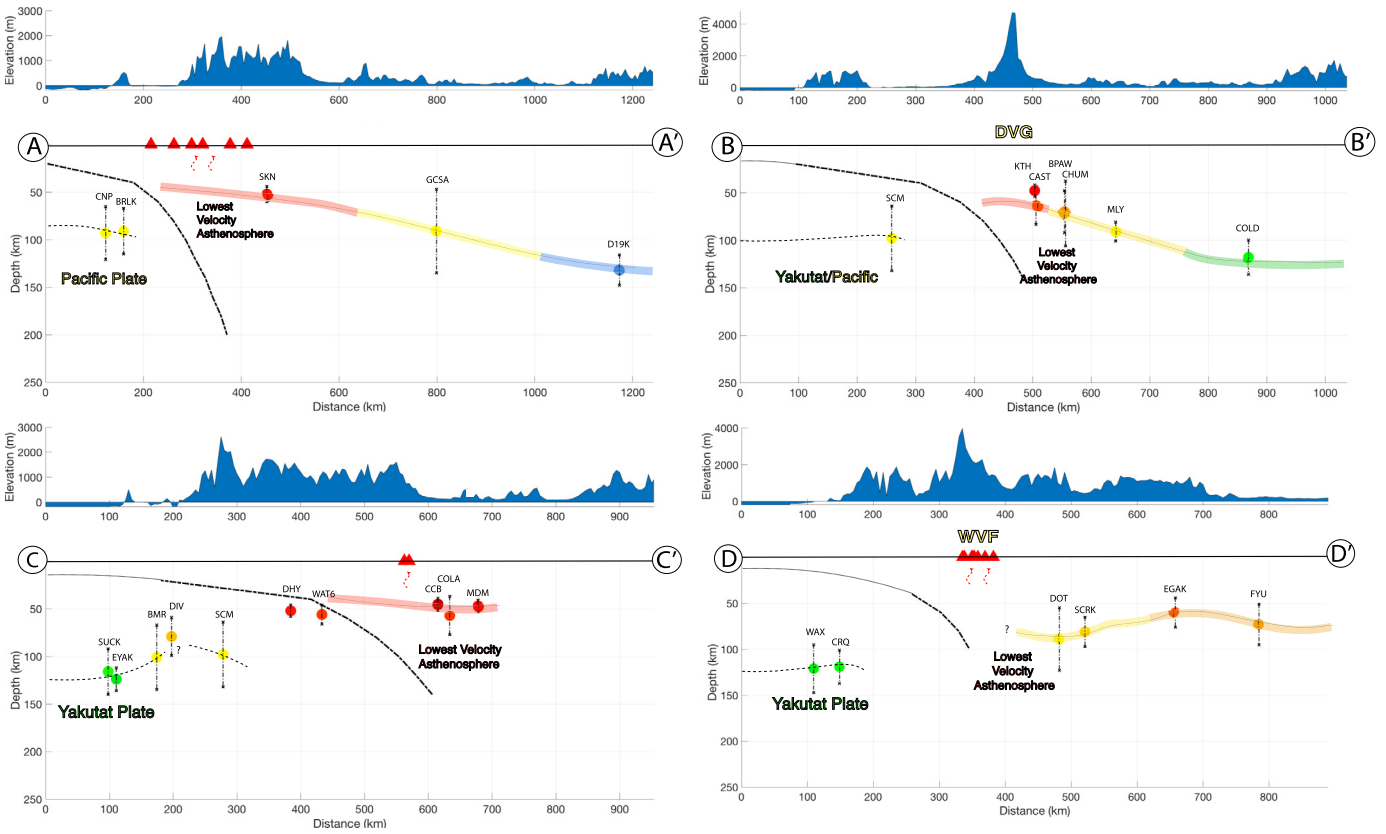

Fig. 8. Cross-sections that represent shear-wave velocity structure beneath Alaska. Cross-section locations are shown in map view in Fig. 5. Colored circles are LAB depths shown at conversion point locations, except for conversions at stations AK.DHY and AK.WAT6 in cross-section C–C′ which likely represent the top of the crust of the subducting plate. Light dashed lines (at the base of the subducting plate) and colored lines (at the base of the upper plate) are our interpretations of LAB shape. Thick dashed lines are the top of the subducting plate from Slab2.0 (Hayes et al., 2018) except in D–D′ where the slab contours are from Kiara Daly, personal communication (2020). Additional discussion of the WVF appears in the supplement. The Denali Volcanic Gap (DVG) location is shown in B–B′. On top of the cross-sections, we show topography from ETOPO1 (Amante and Eakins, 2009). Red triangles represent volcanoes. Both volcanoes and LAB conversion points lie within 0.8 geocentric degrees from the cross-sections.

For example, in the geodynamical models of Rodríguez-González et al. (2012) thicker upper plate lithosphere alters wedge dynamics and reduces slab dip. Following this logic, the relatively thin lithosphere beneath the Seward Peninsula would be associated with the more steeply dipping Pacific plate.

In a different type of model for the DVG, Chuang et al. (2017) propose that low angle subduction produces slab dehydration at anomalously shallow depths, reducing the presence of fluids and the production of partial melt in the mantle wedge. The observed lack of variation in athenospheric velocities between the DVG and surrounding regions is not consistent with this model, unless the proposed variation in fluid and melt content produces no discernible effect on asthenospheric shear-wave velocity.

Our results also shed partial light on the degree to which the upper plate in Alaska is modified by subduction zone processes versus intrinsic lithospheric variations imparted by the original accreted terranes. Our results suggest that both are important. On the one hand, the thick lithosphere in northern Alaska (Fig. 8, Fig. S5), largely made up of the NeoProterozoic-Cambrian northern Arctic-Alaska terrane, has high shear-wave velocities comparable to Archean cratons globally (as discussed above, e.g. Fig. 7b). This cratonic character suggests that the bulk mantle lithospheric properties of the northern Arctic-Alaska terrane differed from those of the terranes to its south at the time that they were accreted, including the nearly adjacent Koyukuk terrane which has been interpreted as oceanic arc lithosphere accreted in the Late Jurassic to early Cretaceous (Colpron et al., 2007; Colpron and Nelson, 2011). On the other hand, subduction processes clearly influence the upper plate at latitudes that at least border the thick northern Arctic Alaska lithosphere. The low asthenospheric shear-wave velocities, thin lithosphere and magmatism beneath the Seward Peninsula are evidence of a subduction influence substantially to the north of the present-day convergent boundaries. In addition, studies of mantle azimuthal anisotropy and regional flow models indicate that mantle flow driven by subduction extends to the latitudes of the northern Arctic Alaska terrane (e.g. Jadamec et al., 2013; Venereau et al., 2019; McPherson et al., 2020).

4.2. Subducting plate properties

Another feature of the shear-wave velocity models is the variation between the thicker subducting lithosphere that lies within the outline of the subducting Yakutat terrane (Fig. 8c–d) and thinner subducting lithosphere with Pacific oceanic crust (Fig. 5). Conversion points sampling the furthest offshore subducting plate with Yakutat crust (Fig. 8c–d) indicate lithosphere that is ∼120 km thick, with maximum values of 122 ± 12 km. In contrast, the conversion point for station SII (Fig. 5), which lies beneath subducting lithosphere with Pacific plate crust at a comparable offshore position relative to subducting slab contours, occurs at 98 ± 16 km. Although only one station in our study captures this offshore distance on the Pacific plate, the LAB depth at this station is comparable to values for Pacific lithosphere near this location from Kumar and Kawakatsu (2011). An apparent difference in incoming plate thickness has also been observed by O'Driscoll and Miller (2015) and Martin-Short et al. (2018).

Variations in crustal thickness explain at least some of the greater total observed thickness of the Yakutat lithosphere. Based on its 20 My age (Müller et al., 2008), the Yakutat lithosphere would actually have a thermally-defined plate thickness that is ∼10 km less than the 40 My-old Pacific lithosphere, assuming a cooling plate model with ∼90 km thick infinite-age lithosphere that matches heat flow data (Hasterok, 2013) and that the base of oceanic lithosphere lies within 50 °C of asthenospheric temperature. However, the thickness of the offshore Yakutat crust is approximately 30 km (Christeson et al., 2013), as opposed to the ∼9 km thick crust of the Pacific plate (Fuis et al., 2008). Thus the ∼21 km thicker crust of the Yakutat plate offsets its ∼10 km thinner thermal mantle, predicting a total thickness that is greater than that of the Pacific plate.

Another facet of subducting plate thickness is that on cross-section C (Fig. 8) the subducting plate carrying Yakutat crust, while ∼120 km offshore, appears to thin as it bends into the trench. Pooling of partial melt below a solidus-related interface near the base of the lithosphere just as it subducts has been invoked beneath Nicaragua from seafloor magnetotelluric data (Naif et al., 2013), and beneath Cascadia in the U.S. from velocity tomography (Hawley et al., 2016). The presence of accumulated melt is one candidate process that could produce the apparent erosion of the base of the Yakutat lithosphere.

As previously mentioned, the negative velocity gradients at depths of 66 km and 58 km beneath stations AK.DHY and AK.WAT6 appear to be related to the top of the subducting plate, based on their location relative to slab seismicity (Fig. 8c). Using Ps receiver function migration, Kim et al. (2014) found a thin layer with reduced velocity that lies close to the AK.DHY and AK.WAT6 conversion points. They interpreted this feature as a layer of thick sediments and high pore fluid pressure between the subducted slab and upper plate (Kim et al., 2014).

5. Conclusions

We employed Bayesian joint inversion of Sp RFs and Rayleigh wave phase velocities to produce shear-wave velocity profiles across Alaska. These new constraints on lithospheric thickness and lithospheric and asthenospheric velocities shed light on several questions.

How has subduction modified upper plate structure? What are the mantle signatures of accreted terranes? A wide band of thin upper plate lithosphere and low velocity asthenosphere extends across central Alaska and the Seward Peninsula. Its spatial correlation with subducting plate seismicity and upper plate magmatic activity indicates that subduction-related fluids and melt have played a key role in thinning the upper plate. In contrast, not only is the lithosphere in and near the northern Arctic Alaska terrane significantly thicker, its mantle has shear-wave velocities that reach values typical of Archean cratons. The latter property suggests that while subduction-related flow may reach these latitudes, possibly thinning the lithosphere, subduction-related processes have not obviously altered the entire mantle lithosphere of the Alaskan interior.

What are the origins of the Denali Volcanic Gap? LAB depths are consistent with Denali Volcanic Gap models involving feedbacks between subduction zone processes and the upper plate. Asthenospheric velocities above the subducting plate within the Denali Volcanic Gap are not significantly different from those beneath adjacent magmatically active regions, suggesting that lower fluxes of slab fluids and reduced wedge partial melt content are not the dominant factor in creating the Denali Volcanic Gap, unless these effects have unobservable impacts on shear-wave velocities.

What differences exist between the subducting plate carrying the Yakutat terrane and the normal Pacific plate lithosphere to the west? The total thickness of the Yakutat lithosphere offshore is about 20 km greater than the Pacific lithosphere, a result which can be explained by the greater thickness of Yakutat crust (Christeson et al., 2013). Thinning of Yakutat lithosphere as it bends into the trench is consistent with erosion of the base of the lithosphere by accumulated partial melt, as has been proposed in Nicaragua and Cascadia (e.g., Naif et al., 2013; Hawley et al., 2016).

CRediT authorship contribution statement

Isabella Gama: Conceptualization, Formal analysis, Methodology, Software, Validation, Visualization, Writing – original draft, Writing – review & editing. **Karen M. Fischer:** Conceptualization, Funding acquisition, Methodology, Project administration, Supervision, Writing – review & editing. **Zachary Eilon:** Conceptualization, Methodology, Software, Writing – review & editing. **Hannah E. Krueger:** Conceptualization, Methodology, Writing – review & editing. **Colleen A. Dalton:** Conceptualization, Funding acquisition, Visualization, Writing – review & editing. **Lucy M. Flesch:** Conceptualization, Funding acquisition.

Declaration of competing interest

The authors declare that they have no known competing financial interests or personal relationships that could have appeared to influence the work reported in this paper.

Acknowledgements

We thank Junlin Hua for great discussions, Michael Mann and Geoffrey A. Abers for volcano and seismicity data. We also thank Lauren Neldner, Ben Davidson, and Dylan Quintal for work on the phase velocities. Rayleigh wave phase velocities will be made available through an open repository. This study employed data from the Alaska Regional Seismic Network (AK, doi:https://doi.org/10.7914/SN/AK), Global Seismograph Network (IU, doi:https://doi.org/10.7914/SN/IU), the USGS Advanced National Seismic System (US doi:https://doi.org/10.7914/SN/US), and the NSF EarthScope Transportable Array (TA, doi:https://doi.org/10.7914/SN/TA). Data were obtained from the IRIS Data Management System. This work was supported by the National Science Foundation ErthScope Program through award EAR-1829401.

Appendix A. Supplementary material

Supplementary material related to this article can be found online at https://doi.org/10.1016/j.epsl.2021.116785.

References

Abers, G.A., Hacker, B.R., 2016. A MATLAB toolbox and Excel workbook for calculating the densities, seismic wave speeds, and major element composition of minerals and rocks at pressure and temperature. Geochem. Geophys. Geosyst. 17 (2), 616–624.

Abers, G.A., Fischer, K.M., Hirth, G., Wiens, D.A., Plank, T., Holtzman, B.K., McCarthy, C., Gazel, E., 2014. Reconciling mantle attenuation-temperature relationships from seismology, petrology, and laboratory measurements. Geochem. Geophys. Geosyst. 15, 3521–3542. https://doi.org/10.1002/2014GC005444.

Amante, C., Eakins, B.W., 2009. ETOPO1 1 Arc-Minute Global Relief Model: Procedures, Data Sources and Analysis. NOAA Technical Memorandum NESDIS NGDC-24. National Geophysical Data Center, NOAA.

Argus, D.F., Gordon, R.G., DeMets, C., 2011. Geologically current motion of 56 plates relative to the no-net rotation reference frame. Geochem. Geophys. Geosyst. 12. https://doi.org/10.1029/2011GC00375.

Babikoff, J.C., Dalton, C.A., 2019. Long-period Rayleigh wave phase velocity tomography using USArray. Geochem. Geophys. Geosyst. 20, 1990–2006. https://doi.org/10.1029/2018GC008073.

Batir, J.F., Blackwell, D.D., Richards, M.C., 2016. Heat flow and temperature-depth curves throughout Alaska: finding regions for future geothermal exploration. J. Geophys. Eng. 13 (3), 366–378. https://doi.org/10.1088/1742-2132/13/3/366.

Berg, E.M., Lin, F.-C., Allam, A., Schulte-Pelkum, V., Ward, K.M., Shen, W., 2020. Shear velocity model of Alaska via joint inversion of Rayleigh wave ellipticity, phase velocities, and receiver functions across the Alaska Transportable Array. J. Geophys. Res., Solid Earth 125, e2019JB018582. https://0120100299/10.1029/2019JB018582.

Brocher, T.M., 2005. Empirical relations between elastic wavespeeds and density in the Earth's crust. Bull. Seismol. Soc. Am. 95 (6), 2081–2092.

Christeson, G.L., Van Avendonk, H.J.A., Gulick, S.P.S., Reece, R.S., Pavlis, G.L., Pavlis, T.L., 2013. Moho interface beneath Yakutat terrane, southern Alaska. J. Geophys. Res., Solid Earth 118, 5084–5097. https://doi.org/10.1002/jgrb.50361.

Chuang, L., Bostock, M., Wech, A., Plourde, A., 2017. Plateau subduction, intraslab seismicity, and the Denali (Alaska) volcanic gap. Geology 45 (7), 647–650. https://doi.org/10.1130/G38867.1.

Colpron, M., Nelson, J.L., 2011. A Digital Atlas of Terranes for the Northern Cordillera. Accessed online from Yukon Geological Survey (www.geology.gov.yk.ca) in 2020.

Colpron, M., Nelson, J.L., Murphy, D.C., 2007. Northern Cordilleran terranes and their interactions through time. GSA Today 17 (4–5), 4–10.

Dziewonski, A.M., Anderson, D.L., 1981. Preliminary reference Earth model. Phys. Earth Planet. Int. 25 (4), 297–356. https://doi.org/10.17611/DP/9991844.

Eberhart-Phillips, D., Christensen, D.H., Brocher, T.M., Hansen, R., Ruppert, N.A., Haeussler, P.J., Abers, G.A., 2006. Imaging the transition from Aleutian subduction to Yakutat collision in central Alaska, with local earthquakes and active source data. J. Geophys. Res., Solid Earth 111 (11), 1–31. https://doi.org/10.1029/2005JB004240.

Eilon, Z., Fischer, K.M., Dalton, C.A., 2018. An adaptive Bayesian inversion for upper-mantle structure using surface waves and scattered body waves. Geophys. J. Int. 214 (1), 232–253. https://doi.org/10.1093/gji/ggy137.

Ekström, G., Abers, G.A., Webb, S.C., 2009. Determination of surface-wave phase velocities across USArray from noise and Aki's spectral formulation. Geophys. Res. Lett. 36 (18), 5–9. https://doi.org/10.1029/2009GL039131.

Feng, L., Ritzwoller, M.H., 2019. A 3-D shear velocity model of the crust and uppermost mantle beneath Alaska including apparent radial anisotropy. J. Geophys. Res., Solid Earth 124 (10), 10468–10497.

Finzel, E.S., Flesch, L.M., Ridgway, K.D., 2011. Kinematics of a diffuse North America–Pacific–Bering plate boundary in Alaska and western Canada. Geology 39 (9), 835–838. https://doi.org/10.1130/G32271.1.

Finzel, E.S., Flesch, L.M., Ridgway, K.D., Holt, W.E., Ghosh, A., 2015. Surface motions and intraplate continental deformation in Alaska driven by mantle flow. Geophys. Res. Lett. 42, 4350–4358. https://doi.org/10.1002/2015GL063987.

French, S., Lekic, V., Romanowicz, B., 2013. Waveform tomography reveals channeled flow at the base of the oceanic asthenosphere. Science 342 (6155), 227–230. https://doi.org/10.1126/science.1241514.

Fuis, G.S., Moore, T.E., Plafker, G., Brocher, T.M., Fisher, M.A., Mooney, W.D., Nokleberg, W.J., Page, R.A., Beaudoin, B.C., Christensen, N.I., Levander, A.R., Lutter, W.J., Saltus, R.W., Ruppert, N.A., 2008. Trans-Alaska crustal transect and continental evolution involving subduction underplating and synchronous foreland thrusting. Geology 36 (3), 267–270. https://doi.org/10.1130/G24257A.1.

Hasterok, D., 2013. A heat flow based cooling model for tectonic plates. Earth Planet. Sci. Lett. 361, 34–43.

Hastings, W.K., 1970. Monte Carlo sampling methods using Markov chains and their applications. Biometrika 57 (1), 97–109.

Hawley, W.B., Allen, R.M., Richards, M.A., 2016. Tomography reveals buoyant asthenosphere accumulating beneath the Juan de Fuca plate. Science 353 (6306), 1406–1408. https://doi.org/10.1126/science.aad8104.

Hayes, G.P., Moore, G.L., Portner, D.E., Hearne, M., Flamme, H., Furtney, M., Smoczyk, G.M., 2018. Slab2, a comprehensive subduction zone geometry model. Science. https://doi.org/10.1126/science.aat4723.

Hua, J., Fischer, K.M., Mancinelli, N.J., Bao, T., 2020. Imaging with pre-stack migration based on Sp scattering kernels. Geophys. J. Int. 220 (1), 428–449.

Jadamec, M.A., Billen, M.I., Roeske, S.M., 2013. Three-dimensional numerical models of flat slab subduction and the Denali fault driving deformation in South-central Alaska. Earth Planet. Sci. Lett. 376, 29–42. https://doi.org/10.1016/j.epsl.2013.06.009.

Jiang, C., Schmandt, B., Ward, K.M., Lin, F.C., Worthington, L.L., 2018. Upper mantle seismic structure of Alaska from Rayleigh and S wave tomography. Geophys. Res. Lett. 45 (19), 10,350–10,359. https://doi.org/10.1029/2018GL079406.

Jin, G., Gaherty, J.B., 2015. Surface wave phase-velocity tomography based on multichannel cross-correlation. Geophys. J. Int. 201 (3), 1383–1398. https://doi.org/10.1093/gji/ggv079.

Keith, C.M., Crampin, S., 1977. Seismic body waves in anisotropic media: synthetic seismograms. Geophys. J. R. Astron. Soc. 49 (1), 225–243. https://doi.org/10.1111/j.1365-246X.1977.tb03710.x.

Kennett, B.L.N., Engdahl, E.R., Buland, R., 1995. Constraints on seismic velocities in the Earth from travel times. Geophys. J. Int. 122, 108–124. https://doi.org/10.1111/j.1365-246X.1995.tb03540.x.

Kim, Y., Abers, G.A., Li, J., Christensen, D., Calkins, J., Rondenay, S., 2014. Alaska megathrust 2: imaging the megathrust zone and Yakutat/Pacific plate interface in the Alaska subduction zone. J. Geophys. Res., Solid Earth 119, 1924–1941. https://doi.org/10.1002/2013JB010581.

Kumar, P., Kawakatsu, H., 2011. Imaging the seismic lithosphere-asthenosphere boundary of the oceanic plate. Geochem. Geophys. Geosyst. 12, Q01006. https://doi.org/10.1029/2010GC003358.

Lin, F-C., Ritzwoller, M.H., Snieder, R., 2009. Eikonal tomography: surface wave tomography by phase front tracking across a regional broad-band seismic array. Geophys. J. Int. 177 (3), 1091–1110.

Martin-Short, R., Allen, R., Bastow, I.D., Porritt, R.W., Miller, M.S., 2018. Seismic imaging of the Alaska subduction zone: implications for slab geometry and volcanism. Geochem. Geophys. Geosyst. 19, 4541–4560. https://doi.org/10.1029/2018GC007962.

Masters, G., Woodhouse, J.H., Freeman, G., 2011. Mineos v1.0.2 [software], computational infrastructure for geodynamics. https://geodynamics.org/cig/software/mineos/.

McPherson, A.M., Christensen, D.H., Abers, G.A., Tape, C., 2020. Shear wave splitting and mantle flow beneath Alaska. J. Geophys. Res., Solid Earth 123, e2019JB018329. https://doi.org/10.1029/2019JB018329.

Miller, M.S., O'Driscoll, L.J., Porritt, R.W., Roeske, S.M., 2018. Multiscale crustal architecture of Alaska inferred from P receiver functions. Lithosphere 10 (2), 267–278. https://doi.org/10.1130/L701.1.

Mosegaard, K., Tarantola, A., 1995. Monte Carlo sampling of solutions to inverse problems. J. Geophys. Res. 100 (B7), 12431–12447.

Müller, R.D., Sdrolias, M., Gaina, C., Roest, W.R., 2008. Age, spreading rates, and spreading asymmetry of the world's ocean crust. Geochem. Geophys. Geosyst. 9, Q04006. https://doi.org/10.1029/2007GC001743.

Naif, S., Key, K., Constable, S., Evans, R.L., 2013. Melt-rich channel observed at the lithosphere–asthenosphere boundary. Nature 495, 356–359. https://doi.org/10.1038/nature11939.

O'Driscoll, L.J., Miller, M.S., 2015. Lithospheric discontinuity structure in Alaska, thickness variations determined by Sp receiver functions. Tectonics 34 (4), 694–714. https://doi.org/10.1002/2014TC003669.

Rodríguez-González, J., Negredo, A.M., Billen, M.I., 2012. The role of the overriding plate thermal state on slab dip variability and on the occurrence of flat subduction. Geochem. Geophys. Geosyst. 13, Q01002. https://doi.org/10.1029/2011GC003859.

Rondenay, S., Montesi, L.G., Abers, G.A., 2010. New geophysical insight into the origin of the Denali volcanic gap. Geophys. J. Int. 182 (2), 613–630. https://doi.org/10.1111/j.1365-246X.2010.04659.x.

Saltus, R.W., Hudson, T.L., 2007. Regional magnetic anomalies, crustal strength, and the location of the northern Cordilleran fold-and-thrust belt. Geology 35 (6), 567–570. https://doi.org/10.1130/G23470A.1.

Stachnik, J., Abers, G.A., Christensen, D., 2004. Seismic attenuation and mantle wedge temperatures in the Alaska subduction zone. J. Geophys. Res. 109, B10304. https://doi.org/10.1029/2004JB003018.

Venereau, C.M.A., Martin-Short, R., Bastow, I.D., Allen, R.M., Kounoudis, R., 2019. The role of variable slab dip in driving mantle flow at the eastern edge of the Alaskan subduction margin: insights from shear-wave splitting. Geochem. Geophys. Geosyst. 20, 2433–2448.

Wang, Y., Tape, C., 2014. Seismic velocity structure and anisotropy of the Alaska subduction zone based on surface wave tomography. J. Geophys. Res., Solid Earth 119 (12), 8845–8865. https://doi.org/10.1002/2014JB011438.

Ward, K.M., Lin, F-C., 2018. Lithospheric structure across the Alaskan Cordillera from the joint inversion of surface waves and receiver functions. J. Geophys. Res., Solid Earth 123 (10), 8780–8797. https://doi.org/10.1029/2018JB015967.

Zhang, Y., Li, A., Hu, H., 2019. Crustal structure in Alaska from receiver function analysis. Geophys. Res. Lett. 46, 1284–1292. https://doi.org/10.1029/2018GL0810111.